Cognitive Neurodynamics (2024) 18:2077–2093
https://doi.org/10.1007/s11571-023-09985-5

RESEARCH ARTICLE

# Effect of adult-born immature granule cells on pattern separation in the hippocampal dentate gyrus

Sang-Yoon Kim[1] · Woochang Lim[1]

Received: 12 January 2023 / Revised: 22 May 2023 / Accepted: 6 June 2023 / Published online: 1 July 2023


## Abstract

Young immature granule cells (imGCs) appear via adult neurogenesis in the hippocampal dentate gyrus (DG). In comparison to mature GCs (mGCs) (born during development), the imGCs exhibit two competing distinct properties such as high excitability (increasing activation degree) and low excitatory innervation (reducing activation degree). We develop a spiking neural network for the DG, incorporating both the mGCs and the imGCs. The mGCs are well known to perform "pattern separation" (i.e., a process of transforming similar input patterns into less similar output patterns) to facilitate pattern storage in the hippocampal CA3. In this paper, we investigate the effect of the young imGCs on pattern separation of the mGCs. The pattern separation efficacy (PSE) of the mGCs is found to vary through competition between high excitability and low excitatory innervation of the imGCs. Their PSE becomes enhanced (worsened) when the effect of high excitability is higher (lower) than the effect of low excitatory innervation. In contrast to the mGCs, the imGCs are found to perform "pattern integration" (i.e., making association between dissimilar patterns). Finally, we speculate that memory resolution in the hippocampal CA3 might be optimally maximized via mixed cooperative encoding through pattern separation and pattern integration.

**Keywords** Hippocampal dentate gyrus · Adult neurogenesis · Immature granule cells · High excitability · Low excitatory innervation · Pattern separation efficacy

## Introduction

The hippocampus, composed of the dentate gyrus (DG) and the subregions CA3 and CA1, plays important roles in memory formation, storage, and retrieval (e.g., episodic and spatial memory) (Squire 1987; Gluck and Myers 2001). In particular, the subregion CA3 has been considered as an autoassociative network, because of extensive recurrent collateral synapses between the pyramidal cells in the CA3 (Marr 1971; McNaughton and Morris 1987; Rolls 1989a, 1989b, 1989c; Willshaw and Buckingham 1990; Treves and Rolls 1991, 1992, 1994; O'Reilly and McClelland 1994). This autoassociative network operates in both the storage and the recall modes. Storage capacity of the autoassociative network implies the number of distinct patterns that can be stored and accurately recalled. Such storage capacity could be increased if the input patterns into the CA3 are sparse (containing few active elements in each pattern) and orthogonalized (nonoverlapping: active elements in one pattern are unlikely to be active in other patterns). This process of transforming a set of input patterns into sparser and orthogonalized patterns is called pattern separation (Marr 1971; McNaughton and Morris 1987; Rolls 1989a, 1989b, 1989c; Willshaw and Buckingham 1990; Treves and Rolls 1991, 1992, 1994; O'Reilly and McClelland 1994; Beck et al. 2000; Nitz and McNaughton 2004; Leutgeb et al. 2007; Bakker et al. 2008; Myers and Scharfman 2009, 2011; Yassa and Stark 2011; Schmidt et al. 2012; Myers et al. 2013; Santoro 2013; Yim et al. 2015; Rolls 2016; Knierim and Neunuebel 2016;

✉ Woochang Lim
wclim@icn.re.kr

Sang-Yoon Kim
sykim@icn.re.kr

[1] Institute for Computational Neuroscience and Department of Science Education, Daegu National University of Education, Daegu 42411, Korea

Scharfman and Myers 2016; Chavlis et al. 2017; Kassab and Alexandre 2018; Dijk and Fenton 2018).

Here, we are concerned about the DG which is the gateway to the hippocampus. The excitatory granule cells (GCs) in the DG receive excitatory inputs from the entorhinal cortex (EC) via the perforant paths (PPs). As a preprocessor for the CA3, the principal GCs perform pattern separation on the input patterns from the EC by sparsifying and orthogonalizing them, and provide the pattern-separated outputs to the pyramidal cells in the CA3 through the mossy fibers (MFs) (Treves and Rolls 1994; O'Reilly and McClelland 1994; Myers and Scharfman 2009, 2011; Schmidt et al. 2012; Myers et al. 2013; Yim et al. 2015; Rolls 2016; Knierim and Neunuebel 2016; Scharfman and Myers 2016; Chavlis et al. 2017; Kassab and Alexandre 2018). Then, a new pattern may be stored in modified collateral synapses between the pyramidal cells in the hippocampal CA3. In this way, pattern separation in the DG could facilitate pattern storage in the hippocampal CA3.

The whole GCs are grouped into the lamellar clusters (Andersen et al. 1971; Amaral and Witter 1989; Andersen et al. 2000; Sloviter and Lømo 2012). In each cluster, there exist one inhibitory basket cell (BC) and one inhibitory HIPP (hilar perforant path-associated) cell, together with excitatory GCs. During pattern separation, the GCs show sparse firing activity via the winner-take-all competition (Coultrip et al. 1992; Almeida et al. 2009; Petrantonakis and Poirazi 2014, 2015; Houghton 2017; Espinoza et al. 2018; Su et al. 2019; Barranca et al. 2019; Bielczyk et al. 2019; Wang et al. 2020; Kim and Lim 2022a). Only strongly active GCs survive under the feedback inhibitory inputs from the BC and the HIPP cell. We note that, sparsity (resulting from strong feedback inhibition) has been considered to improve the pattern separation efficacy (Treves and Rolls 1994; O'Reilly and McClelland 1994; Myers and Scharfman 2009, 2011; Schmidt et al. 2012; Myers et al. 2013; Rolls 2016; Knierim and Neunuebel 2016; Scharfman and Myers 2016; Chavlis et al. 2017; Kassab and Alexandre 2018).

One of the most distinctive characteristics of the DG is occurrence of adult neurogenesis which results in the generation of new GCs during adulthood. Altman's pioneering studies in adult rat and cat brains for the adult neurogenesis were done decades ago in the 1960 s (Altman 1962, 1963; Altman and Das 1965). Since then, adult neurogenesis has been shown to be a robust phenomenon, occurring in most mammals, mainly in the subgranular zone of the DG and the subventricular zone of the lateral ventricles (Bayer 2016; Ming and Song 2011; Christian et al. 2020). The new GCs born in the subgranular zone migrate into the granular layer of the DG. The whole population of GCs is thus composed of mature GCs (mGCs) born during the development and adult-born immature GCs (imGCs). In contrast to the mGCs, the young adult-born imGCs are known to have marked properties such as high excitability, weak inhibition, and low excitatory innervation (Aimone et al. 2009, 2010, 2011; Sahay et al. 2011a, 2011b; Finnegan and Becker 2015).

The adult-born imGCs show gradual continuous maturation process (Heigele et al. 2016; Jahn and Bergami 2018; Murray et al. 2020). For 0–2 weeks of age, the imGCs undergo early survival competition and begin axonal extension. Then, for 3–4 weeks of age, the synapses and dendrites of the imGCs begin to gradually appear and receive excitatory inputs. In this maturation stage of about 3–4 weeks, the imGCs exhibit highly excitability, less inhibition, and low excitatory innervation. From the 5th week of age, the imGCs become more matured, and eventually, at about 8 weeks of age, the imGCs become almost mature, which is essentially indistinguishable from mGCs. Here, we consider young imGCs with 3–4 weeks of age, showing two competing properties such as high excitability and low excitatory innervation; for simplicity, we approximately neglect inhibition of the imGCs in our DG network.

In this paper, we develop a spiking neural network for the DG, including both mGCs and imGCs. We choose the fraction of imGCs ($F^{(im)}$) in our DG network as $F^{(im)} = 10\ \%$, based on quantitative previous studies (Cameron and Mckay 2001; van Praag et al. 2002; Laplagne et al. 2006, 2007; Toni et al. 2007, 2008; Imayoshi et al. 2008; Gu et al. 2012; Nakashiba et al. 2012; Myers et al. 2013), showing that about 4–10 % of the whole GCs are imGCs. In Sect. 4, we also consider another case of $F^{(im)} = 5\ \%$ to examine the effect of fraction of imGCs on our main results. As shown in Fig. 6b, our main conclusion is insensitive to the fraction of imGCs.

As is well known, sparsity (sparse coding) may improve pattern separation (transforming similar input patterns into less similar output patterns) (Myers and Scharfman 2009; Chavlis et al. 2017). Based on this mechanism, we investigate the effect of young imGCs on pattern separation of the mGCs in our DG network. Their pattern separation efficacy is found to change via competition between high excitability (increasing activation degree) and low excitatory innervation (reducing activation degree) of the imGCs. When the effect of high excitability (low excitatory innervation) is larger, the pattern separation efficacy of the mGCs becomes enhanced (worsened) due to increased (decreased) feedback inhibition to the mGCs [caused by increased (decreased) activation of the imGCs]. We also note that the imGCs perform pattern integration (i.e., making association between dissimilar patterns), in

contrast to the mGCs (pattern separators). It is speculated that memory resolution (corresponding to the extent of information incorporated into memories) in the hippocampal CA3 might be optimally maximized through mixed cooperative encoding via pattern separation of the mGCs and pattern integration of the imGCs.

This paper is organized as follows. In Sect. 2, we describe a spiking neural network for the adult neurogenesis in the hippocampal DG. Then, in the main Sect. 3, we investigate the effect of young imGCs on pattern separation of the mGCs. Finally, we give summary and discussion in Sect. 4.

## Spiking neural network for the adult neurogenesis in the dentate gyrus

In this section, we describe our spiking neural network for the adult neurogenesis in the DG. Based on the anatomical and the physiological properties described in Myers and Scharfman (2009, 2011); Chavlis et al. (2017), we developed the DG spiking neural networks in the works for the winner-take-all competition (Kim and Lim 2022a), the sparsely synchronized rhythm (Kim and Lim 2022b), and the pattern separation (Kim and Lim 2022c). Here, we first refine our prior spiking neural networks to include more synaptic connections with a high degree of anatomical and physiological realism (Santhakumar et al. 2005; Morgan et al. 2007), and then incorporate the young adult-born imGCs to complete structure of our spiking neural network for the adult neurogenesis.

Obviously, our spiking neural network will not capture all the detailed anatomical and physiological complexity of the DG. But, with a limited number of essential elements and synaptic connections in our DG network, effect of the imGCs on the pattern separation could be successfully studied. Hence, our spiking neural network model would build a foundation upon which additional complexity may be added and guide further research.

### Architecture of the spiking neural network of The DG

Figure 1 shows (a) schematic representation of major cells and synaptic connections in our DG network incorporating adult-born imGCs and (b) the box diagram for the DG network with 3 types of lamellar (blue), cross-lamellar (red), and random (black) synaptic connections. In our DG network, the fraction of imGCs is 10 % in the whole population of GCs, high excitability of the imGCs is considered, there are no inhibitory inputs into the imGCs, and their low excitatory innervation is also taken into consideration (Aimone et al. 2009, 2010, 2011; Sahay et al. 2011a, b; Finnegan and Becker 2015; Dieni et al. 2016).

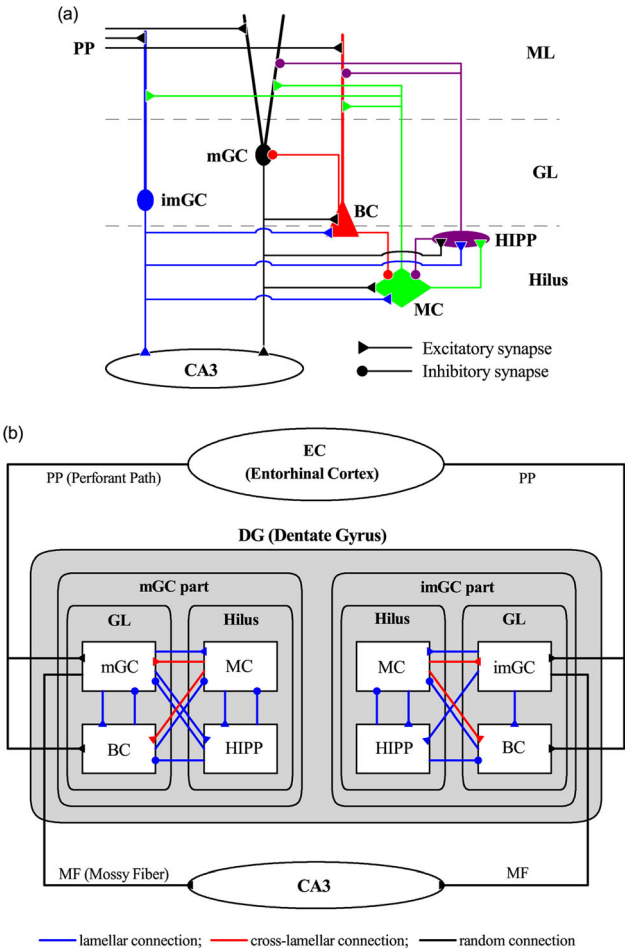


**Fig. 1** Spiking neural network for the hippocampal dentate gyrus (DG). (**a**) Schematic representation of major cells and synaptic connections in our DG network incorporating adult-born immature GCs (imGCs). Fraction of the imGCs is 10 % in the whole population of GCs. Note that there are no inhibitory inputs into the imGCs, in contrast to the case of mGCs. Here, BC, MC, HIPP, PP, GL, and ML represent the basket cell, the mossy cell, the hilar perforant path-associated cell, perforant path, granular layer, and molecular layer, respectively. (**b**) Box diagram for our DG network with 3 types of synaptic connections. Blue, red, and black lines represent lamellar, cross-lamellar, and random connections, respectively. (Color figure online)

In the DG, we consider the granular layer (GL), composed of the excitatory mGCs and imGCs and the inhibitory BCs, and the underlying hilus, consisting of the excitatory MCs and the inhibitory HIPP cells, whose axons project to the upper molecular layer (ML). We note that there are two types of excitatory cells, GCs and MCs, in contrast to the case of the CA3 and CA1 with only one type of excitatory pyramidal cells.

From the outside of the DG, the EC provides the external excitatory inputs randomly to the mGCs, the imGCs, and the inhibitory BCs (with dendrites extending to the outer ML) via PPs (Myers and Scharfman 2009, 2011; Myers et al. 2013; Scharfman and Myers 2016; Chavlis et al. 2017). Thus, both the mGCs and the imGCs receive direct excitatory EC input via PPs (EC → mGC and imGCs) through random connections in Fig. 1b. The connection probability $p_c$ for EC → mGC and BC is 20 %, while $p_c$ for EC → imGC is decreased to 20 $x$ % [$x$ (synaptic connectivity fraction); $0 \le x \le 1$] due to low excitatory innervation. Moreover, only the mGCs receive indirect feedforward inhibitory input, mediated by the BCs (EC → BC → mGC).

In the GL, the whole GCs (i.e., both the mGCs and the imGCs) are grouped into lamellar clusters (Andersen et al. 1971; Amaral and Witter 1989; Andersen et al. 2000; Sloviter and Lømo 2012), and one inhibitory BC exists in each cluster. Here, the BC (receiving excitation from the whole GCs in the same cluster) provides the feedback inhibition to only all the mGCs via lamellar connections in Fig. 1b; a primary mGC-BC feedback loop is formed. Thus, in each cluster the BC provides both the feedforward and the feedback inhibition to all the mGCs in the same cluster.

In the hilus, we also consider lamellar organization for the MCs and HIPP cells (Myers and Scharfman 2011; Myers et al. 2013; Scharfman and Myers 2016; Jinde et al. 2013) (i.e., all the MCs and the HIPP cells in the hilus also are grouped into lamellar clusters). As in the case of BC, the HIPP cell receives excitation from the whole GCs in the same cluster, and projects the feedback inhibition to all the mGCs in the same cluster through lamellar connections; a secondary mGC-HIPP feedback loop is formed. Thus, there appear two kinds of feedback loops of mGC-BC and mGC-HIPP.

In our DG network, the MCs play the role of "controller" for the activities of the two feedback loops of mGC-BC and mGC-HIPP. Each MC in a cluster receives excitation from the whole GCs in the same cluster (lamellar connection), while it makes excitatory projection randomly to the mGCs and the imGCs in other clusters via cross-lamellar connections (Jinde et al. 2013). The connection probability $p_c$ for MC → mGC is 20 %, while $p_c$ for MC → imGC is decreased to 20 $x$ % ($0 \le x \le 1$) because of low excitatory innervation. Thus, the GC-MC driving loop for determining the activities of the controller MCs is formed.

The MCs control the activities of the feedback loops of mGC-BC and mGC-HIPP. Each MC in a cluster receives inhibition from the BC and the HIPP cell in the same cluster (lamellar connection). Then, the MCs in the cluster project excitation to the BCs in other clusters through cross-lamellar connections (the connection probability $p_c$ for MC → BC is 20 %) (Jinde et al. 2013), while they provide excitation to the HIPP cell in the same cluster (lamellar connection). Thus, two "control" loops of MC-BC and MC-HIPP, controlling the activities of the two feedback loops of mGC-BC and mGC-HIPP, are formed. Finally, the HIPP cell inhibits the BC in the same cluster (lamellar connection for HIPP → BC); there are no reverse synaptic connections for BC → HIPP (Santhakumar et al. 2005; Morgan et al. 2007). Thus, the activity of the BC in a cluster is controlled through excitation from the MCs in other clusters (cross-lamellar connections) and inhibition from the HIPP cell in the same cluster (lamellar connection).

The mGCs in a cluster exhibit sparse firing activity via the winner-take-all competition (Coultrip et al. 1992; Almeida et al. 2009; Petrantonakis and Poirazi 2014, 2015; Houghton 2017; Espinoza et al. 2018; Su et al. 2019; Barranca et al. 2019; Bielczyk et al. 2019; Wang et al. 2020; Kim and Lim 2022a). Only strongly active mGCs may survive under the feedback inhibition from the BC and the HIPP cell in the same cluster. Here, the activities of the BC and the HIPP cell are controlled by the controller MCs; in the case of BC, the HIPP cell also inhibits it. On the other hand, the imGCs receive no inhibition. Particularly, due to their low firing threshold, they become highly active, in contrast to the case of mGCs (Aimone et al. 2009, 2010, 2011; Sahay et al. 2011a, 2011b; Finnegan and Becker 2015; Dieni et al. 2016). However, when considering their low excitatory innervation from the EC cells and the MCs, their firing activity is reduced (Finnegan and Becker 2015; Dieni et al. 2016).

Based on the anatomical information given in Myers and Scharfman (2009, 2011); Myers et al. (2013); Scharfman and Myers (2016); Chavlis et al. (2017), we choose the numbers of the GCs, BCs, MCs, and HIPP cells in the DG and the EC cells. As in our prior works (Kim and Lim 2022a, 2022b, 2022c), we develop a scaled-down spiking neural network where the total number of excitatory GCs ($N_{GC}$) is 2,000, corresponding to $\frac{1}{500}$ of the $10^6$ GCs found in rats (West et al. 1991). The fraction of imGCs in the whole population of the GCs is 10 %, and hence the number of the imGCs (mGCs) is 200 (1800). The whole GCs (i.e., mGCs and imGCs) are grouped into the $N_c$ (= 20) lamellar clusters (Andersen et al. 1971; Amaral and Witter 1989; Andersen et al. 2000; Sloviter and Lømo 2012). Then, in each cluster, there are $n_{GC}^{(c)}$ (= 100) GCs (i.e., 90 mGC and 10 imGCs) and one inhibitory BC (Myers and Scharfman 2011; Myers et al. 2013; Scharfman and Myers 2016). As a result, the number of the BCs ($N_{BC}$) in the whole DG network becomes 20, corresponding to 1/100 of $N_{GC}$ (Buckmaster et al. 1996; Nomura et al.

1997a, 1997b; Buckmaster and Jongen-Rêlo 1999; Buckmaster et al. 2002; Morgan et al. 2007).

The EC layer II projects the excitatory inputs to the mGCs, the imGCs, and the BCs via the PPs through random connections (Myers and Scharfman 2009, 2011; Myers et al. 2013; Scharfman and Myers 2016; Chavlis et al. 2017). The estimated number of the EC layer II cells ($N_{\rm EC}$) is about 200,000 in rats, which corresponds to 20 EC cells per 100 GCs (Amaral et al. 1990). Hence, we choose $N_{\rm EC} = 400$ in our DG network. Also, the activation degree of the EC cells is chosen as 10 % (McNaughton et al. 1991). Thus, we randomly choose 40 active ones among the 400 EC cells. Each active EC cell is modeled in terms of the Poisson spike train with frequency of 40 Hz (Hafting et al. 2005).

Next, we consider the hilus, composed of the excitatory MCs and the inhibitory HIPP cells (Scharfman and Myers 2013; Scharfman 2018; Lübke et al. 1998; Amaral et al. 2007; Jinde et al. 2012, 2013; Ratzliff et al. 2004). In rats, the number of MCs ($N_{\rm MC}$) is known to change from 30,000 to 50,000, and the estimated number of HIPP cells ($N_{\rm HIPP}$) is about 12,000 (Buckmaster and Jongen-Rêlo 1999). In our scaled-down DG network, we choose $N_{\rm MC} = 60$ and $N_{\rm HIPP} = 20$. All the MCs and the HIPP cells are also grouped into the 20 lamellar clusters, as in the case of the GCs and the BCs. Hence, in each cluster, there are $n_{\rm MC}^{(c)}$ (= 3) MCs and one HIPP cell (Myers and Scharfman 2011; Myers et al. 2013; Scharfman and Myers 2016).

With the above information on the numbers of the relevant cells and the synaptic connections between them, we develop a one-dimensional ring network for the adult neurogenesis in the DG, as in our prior works (Kim and Lim 2022a, 2022b, 2022c); e.g., refer to Fig. 1b1, b2, b3 in Kim and Lim (2022c) for the schematic diagrams of the ring networks. Due to the ring structure, our spiking neural network has advantage for computational efficiency, and its visual representation may also be easily made.

## Single neuron models and synaptic currents in the DG spiking neural network

As elements of our DG spiking neural network for the adult neurogenesis, we choose leaky integrate-and-fire (LIF) neuron models with additional afterhyperpolarization (AHP) currents which determines refractory periods, as in our prior DG networks (Kim and Lim 2022a, 2022b, 2022c). This LIF neuron model is one of the simplest spiking neuron models (Gerstner and Kistler 2002). Due to its simplicity, it may be easily analyzed and simulated. It has thus been very popularly used as a spiking neuron model.

The governing equations for evolutions of dynamical states of individual cells in the $X$ population are as follows:

$$C_X \frac{dv_i^{(X)}(t)}{dt} = -I_{L,i}^{(X)}(t) - I_{AHP,i}^{(X)}(t) + I_{ext}^{(X)} - I_{syn,i}^{(X)}(t), \quad i = 1, \cdots, N_X, \tag{1}$$

where $N_X$ is the total number of cells in the $X$ population, $X$ = mGC, imGC, and BC in the granular layer and $X$ = MC and HIPP in the hilus. In Eq. (1), $C_X$ (pF) represents the membrane capacitance of the cells in the $X$ population, and the dynamical state of the $i$th cell in the $X$ population at a time $t$ (ms) is characterized by its membrane potential $v_i^{(X)}(t)$ (mV). We note that the time-evolution of $v_i^{(X)}(t)$ is governed by 4 types of currents (pA) into the $i$th cell in the $X$ population; the leakage current $I_{L,i}^{(X)}(t)$, the AHP current $I_{AHP,i}^{(X)}(t)$, the external constant current $I_{ext}^{(X)}$ (independent of $i$), and the synaptic current $I_{syn,i}^{(X)}(t)$.

The equation for a single LIF neuron model (without the AHP current and the synaptic current) describes a simple parallel resistor-capacitor (RC) circuit. In this case, the 1st type of leakage current is due to the resistor and the integration of the external current is due to the capacitor which is in parallel to the resistor. When its membrane potential reaches a threshold, a neuron fires a spike, and then the 2nd type of AHP current follows. As the decay time of the AHP current is increased, the refractory period becomes longer. Here, we consider a subthreshold case where the 3rd type of external constant current is zero (i.e., $I_{ext}^{(X)} = 0$) (Chavlis et al. 2017).

The 1st type of leakage current $I_{L,i}^{(X)}(t)$ for the $i$th cell in the $X$ population is given by:

$$I_{L,i}^{(X)}(t) = g_L^{(X)}(v_i^{(X)}(t) - V_L^{(X)}), \tag{2}$$

where $g_L^{(X)}$ and $V_L^{(X)}$ denote conductance (nS) and reversal potential for the leakage current, respectively. The $i$th cell fires a spike when its membrane potential $v_i^{(X)}$ reaches a threshold $v_{th}^{(X)}$ at a time $t_{f,i}^{(X)}$. Then, the 2nd type of AHP current $I_{AHP,i}^{(X)}(t)$ follows after spiking (i.e., $t \geq t_{f,i}^{(X)}$),:

$$I_{AHP,i}^{(X)}(t) = g_{AHP}^{(X)}(t)\ (v_i^{(X)}(t) - V_{AHP}^{(X)}) \quad \text{for} \quad t \geq t_{f,i}^{(X)}. \tag{3}$$

Here, $V_{AHP}^{(X)}$ represents the reversal potential for the AHP current, and the conductance $g_{AHP}^{(X)}(t)$ is given by an exponential-decay function:

$$g_{AHP}^{(X)}(t) = \bar{g}_{AHP}^{(X)}\ e^{-(t-t_{f,i}^{(X)})/\tau_{AHP}^{(X)}}, \tag{4}$$

where $\bar{g}_{AHP}^{(X)}$ and $\tau_{AHP}^{(X)}$ denote the maximum conductance and the decay time constant for the AHP current,

respectively. With increasing $\tau_{AHP}^{(X)}$, the refractory period becomes longer.

The parameter values of the capacitance $C_X$, the leakage current $I_L^{(X)}(t)$, and the AHP current $I_{AHP}^{(X)}(t)$ are the same as those in our prior DG networks (Kim and Lim 2022a, 2022b, 2022c), and refer to Table 1 in Kim and Lim (2022a). These parameter values are based on physiological properties of the GC, BC, MC, and HIPP cell (Lübke et al. 1998; Chavlis et al. 2017).

We note that, the GC in Table 1 in Kim and Lim (2022a) corresponds to the mGC. The imGCs also have the same parameter values as those of the mGC, except for the leakage reversal potential $V_L$. The mGC with $V_L = -75$ mV exhibits a spiking transition when passing a threshold $I^* = 80$ mV. Here, we consider a case that the imGC has an increased leakage reversal potential of $V_L = -72$ mV, which could lead to intrinsic high excitability. Then, it shows a firing transition when passing $I^* = 69.7$ pA. In this way, the imGC may have a lower firing threshold (Sahay et al. 2011a, 2011b; Aimone et al. 2011, 2009), which is well shown in Fig. 2 for the $f - I$ (i.e., firing rate-current) curves of the mGC (red curve) and the imGC (blue curve).

Next, we consider the 4th type of synaptic current $I_{syn,i}^{(X)}(t)$ into the $i$th cell in the $X$ population, composed of the following 3 types of synaptic currents:

$$I_{syn,i}^{(X)}(t) = I_{\mathrm{AMPA,i}}^{(X,Y)}(t) + I_{\mathrm{NMDA,i}}^{(X,Y)}(t) + I_{\mathrm{GABA,i}}^{(X,Z)}(t). \quad (5)$$

Here, $I_{\mathrm{AMPA,i}}^{(X,Y)}(t)$ and $I_{\mathrm{NMDA,i}}^{(X,Y)}(t)$ are the excitatory AMPA (α-amino-3-hydroxy-5-methyl-4-isoxazolepropionic acid) receptor-mediated and NMDA (*N*-methyl-*D*-aspartate) receptor-mediated currents from the presynaptic source $Y$ population to the postsynaptic $i$th neuron in the target $X$ population, respectively. In contrast, $I_{\mathrm{GABA,i}}^{(X,Z)}(t)$ is the inhibitory $GABA_A$ ($\gamma$-aminobutyric acid type A) receptor-mediated current from the presynaptic source $Z$ population to the postsynaptic $i$th neuron in the target $X$ population.

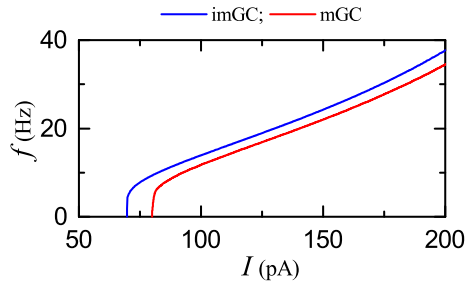


**Fig. 2** Firing transitions of mature GCs (mGCs) and adult-born immature GCs (imGCs). $f - I$ ($f$ : firing rate and $I$ : current) curve for the mGC (red line) and the imGC (blue line). (Color figure online)

Like the case of the AHP current, the $R$ (= AMPA, NMDA, or GABA) receptor-mediated synaptic current $I_{R,i}^{(T,S)}(t)$ from the presynaptic source $S$ population to the $i$th postsynaptic cell in the target $T$ population is given by:

$$I_{R,i}^{(T,S)}(t) = g_{R,i}^{(T,S)}(t)\ (v_i^{(T)}(t) - V_R^{(S)}). \quad (6)$$

Here, $g_{(R,i)}^{(T,S)}(t)$ and $V_R^{(S)}$ represent synaptic conductance (nS) and synaptic reversal potential (mV) (determined by the type of the presynaptic source $S$ population), respectively.

In the case of the $R$ (=AMPA and GABA)-mediated synaptic currents, we get the synaptic conductance $g_{R,i}^{(T,S)}(t)$ from:

$$g_{R,i}^{(T,S)}(t) = K_R^{(T,S)} \sum_{j=1}^{N_S} w_{ij}^{(T,S)}\ s_j^{(T,S)}(t), \quad (7)$$

where $K_R^{(T,S)}$ is the synaptic strength per synapse for the $R$-mediated synaptic current from the $j$th presynaptic neuron

**Table 1** Parameters for the synaptic currents $I_R^{(\mathrm{GC,S})}(t)$ into the GCs (granule cells). The whole population of the GCs is composed of a major subpopulation of mGCs (mature GCs) and a minor subpopulation of imGCs (immature GCs). Both the mGCs and the imGCs receive the excitatory inputs from the EC (entorhinal cortex) cells and the hilar MCs (mossy cells); synaptic parameters for the excitatory inputs are valid for both the mGCs and the imGCs. In addition, the mGCs receive the feedforward and feedback inhibitory inputs from the BCs (basket cells) and the feedback inhibitory input from the HIPP (hilar perforant path-associated) cells, while there are no inhibitory inputs into the imGCs

| Target cells ($T$) | GC | | | | | |
|---|---|---|---|---|---|---|
| Source cells ($S$) | EC | | BC | HIPP | MC | |
| Receptor ($R$) | AMPA | NMDA | GABA | GABA | AMPA | NMDA |
| $K_R^{(T,S)}$ | 0.89 | 0.15 | 15.0 | 3.0 | 0.07 | 0.01 |
| $\tau_{R,r}^{(T,S)}$ | 0.1 | 0.33 | 0.9 | 0.5 | 0.1 | 0.33 |
| $\tau_{R,d}^{(T,S)}$ | 2.5 | 50.0 | 6.8 | 6.0 | 2.5 | 50.0 |
| $\tau_{R,l}^{(T,S)}$ | 3.0 | 3.0 | 0.85 | 1.6 | 3.0 | 3.0 |
| $V_R^{(S)}$ | 0.0 | 0.0 | − 86.0 | − 86.0 | 0.0 | 0.0 |

in the source $S$ population to the $i$th postsynaptic cell in the target $T$ population. The inter-population synaptic connection from the source $S$ population (with $N_s$ cells) to the target $T$ population is given by the connection weight matrix $W^{(T,S)}$ $(= \{w_{ij}^{(T,S)}\})$ where $w_{ij}^{(T,S)} = 1$ if the $j$th cell in the source $S$ population is presynaptic to the $i$th cell in the target $T$ population; otherwise $w_{ij}^{(T,S)} = 0$. The fraction of open ion channels at time $t$ is also represented by $s^{(T,S)}(t)$.

In contrast, in the NMDA-receptor case, some of the postsynaptic NMDA channels are blocked by the positive magnesium ion $Mg^{2+}$ (Jahr and Stevens 1990). Hence, the conductance in the case of NMDA receptor is given by Chavlis et al. (2017):

$$g_{R,i}^{(T,S)}(t) = \widetilde{K}_R^{(T,S)} f(v^{(T)}(t)) \sum_{j=1}^{N_S} w_{ij}^{(T,S)} s_j^{(T,S)}(t). \tag{8}$$

Here, $\widetilde{K}_R^{(T,S)}$ is the synaptic strength per synapse, and the fraction of NMDA channels that are not blocked by the $Mg^{2+}$ ion is given by a sigmoidal function $f(v^{(T)}(t))$:

$$f(v^{(T)}(t)) = \frac{1}{1 + \eta \cdot [Mg^{2+}]_o \cdot \exp(-\gamma \cdot v^{(T)}(t))}. \tag{9}$$

Here, $v^{(T)}(t)$ is the membrane potential of the target cell, $[Mg^{2+}]_o$ is the outer $Mg^{2+}$ concentration, $\eta$ denotes the sensitivity of $Mg^{2+}$ unblock, $\gamma$ represents the steepness of $Mg^{2+}$ unblock, and the values of parameters change depending on the target cell (Chavlis et al. 2017). For simplicity, some approximation to replace $f(v^{(T)}(t))$ with $\langle f(v^{(T)}(t)) \rangle$ [i.e., time-averaged value of $f(v^{(T)}(t))$ in the range of $v^{(T)}(t)$ of the target cell] has been done in Kim and Lim (2022b). Then, an effective synaptic strength $K_{\mathrm{NMDA}}^{(T,S)} (= \widetilde{K}_{\mathrm{NMDA}}^{(T,S)} \langle f(v^{(T)}(t)) \rangle)$ was introduced by absorbing $\langle f(v^{(T)}(t)) \rangle$ into $K_{\mathrm{NMDA}}^{(T,S)}$. Thus, with the scaled-down effective synaptic strength $K_{\mathrm{NMDA}}^{(T,S)}$ (containing the blockage effect of the $Mg^{2+}$ ion), the conductance $g$ for the NMDA receptor may also be well approximated in the same form of conductance as the other AMPA and GABA receptors in Eq. (7). Thus, we get all the effective synaptic strengths $K_{\mathrm{NMDA}}^{(T,S)}$ from the synaptic strengths $\widetilde{K}_{\mathrm{NMDA}}^{(T,S)}$ in Chavlis et al. (2017) by considering the average blockage effect of the $Mg^{2+}$ ion. Consequently, we can use the same form of synaptic conductance of Eq. (7) in all the cases of $R =$ AMPA, NMDA, and GABA.

The postsynaptic ion channels are opened through binding of neurotransmitters (emitted from the source $S$ population) to receptors in the target $T$ population. The fraction of open ion channels at time $t$ is represented by $s^{(T,S)}(t)$. The time course of $s_j^{(T,S)}(t)$ of the $j$th cell in the source $S$ population is given by a sum of double exponential functions $E_R^{(T,S)}(t - t_f^{(j)} - \tau_{R,l}^{(T,S)})$:

$$s_j^{(T,S)}(t) = \sum_{f=1}^{F_j^{(s)}} E_R^{(T,S)}(t - t_f^{(j)} - \tau_{R,l}^{(T,S)}). \tag{10}$$

Here, $t_f^{(j)}$ and $F_j^{(s)}$ are the $f$th spike time and the total number of spikes of the $j$th cell in the source $S$ population, respectively, and $\tau_{R,l}^{(T,S)}$ is the synaptic latency time constant for $R$-mediated synaptic current. The double exponential-decay function $E_R^{(T,S)}(t)$ (corresponding to contribution of a presynaptic spike occurring at $t = 0$ in the absence of synaptic latency) is given by:

$$E_R^{(T,S)}(t) = \frac{1}{\tau_{R,d}^{(T,S)} - \tau_{R,r}^{(T,S)}} \left( e^{-t/\tau_{R,d}^{(T,S)}} - e^{-t/\tau_{R,r}^{(T,S)}} \right) \cdot \Theta(t). \tag{11}$$

Here, $\Theta(t)$ is the Heaviside step function: $\Theta(t) = 1$ for $t \geq 0$ and 0 for $t < 0$, and $\tau_{R,r}^{(T,S)}$ and $\tau_{R,d}^{(T,S)}$ are synaptic rising and decay time constants of the $R$-mediated synaptic current, respectively.

In comparison with our prior DG networks (Kim and Lim 2022a, 2022b, 2022c), we include more synaptic connections with a high degree of anatomical and physiological realism (Santhakumar et al. 2005; Morgan et al. 2007), and incorporate the imGCs. Thus, a new feedforward inhibition, mediated by the BCs, is provided to the mGCs, and there appear two feedback loops of mGC-BC and mGC-HIPP, (projecting feedback inhibition to the mGCs), the activities of which are controlled by the two control loops of MC-BC and MC-HIPP (MCs: controllers).

Finally, we present the parameter values for the synaptic strength per synapse $K_R^{(T,S)}$, the synaptic rising time constant $\tau_{R,r}^{(T,S)}$, synaptic decay time constant $\tau_{R,d}^{(T,S)}$, synaptic latency time constant $\tau_{R,l}^{(T,S)}$, and the synaptic reversal potential $V_R^{(S)}$ for the synaptic currents into the GCs (i.e., both mGCs and imGCs) and the BCs in the GL, in Tables 1 and 2, respectively, and for the synaptic currents into the MCs and the HIPP cells in Table 3. These parameter values are also based on the physiological properties of the relevant cells (Kneisler and Dingledine 1995; Geiger et al. 1997; Bartos et al. 2001; Santhakumar et al. 2005; Morgan et al. 2007; Schmidt-Hieber et al. 2007; Larimer and Strowbridge 2008; Schmidt-Hieber and Bischofberger 2010; Krueppel et al. 2011; Chiang et al. 2012; Chavlis et al. 2017).

All of our source codes for computational works were written in C programming language. Numerical integration of the governing equation for the time-evolution of states

**Table 2** Parameters for the synaptic currents $I_R^{(\mathrm{BC,S})}(t)$ into the BCs (basket cells). The BCs receive the excitatory inputs from the EC (entorhinal cortex) cells, the GCs (granulce cells; both mGCs and imGCs) and the MCs (mossy cells) and the inhibitory input from the HIPP (hilar perforant path-associated) cells

| Target cells ($T$) | BC | | | | | | |
|---|---|---|---|---|---|---|---|
| Source cells ($S$) | EC | | GC | | MC | | HIPP |
| Receptor ($R$) | AMPA | NMDA | AMPA | NMDA | AMPA | NMDA | GABA |
| $K_R^{(T,S)}$ | 0.75 | 0.13 | 0.38 | 0.02 | 6.14 | 0.36 | 9.22 |
| $\tau_{R,r}^{(T,S)}$ | 2.0 | 6.6 | 2.5 | 10.0 | 2.5 | 10.0 | 0.4 |
| $\tau_{R,d}^{(T,S)}$ | 6.3 | 126.0 | 3.5 | 130.0 | 3.5 | 130.0 | 5.8 |
| $\tau_{R,l}^{(T,S)}$ | 3.0 | 3.0 | 0.8 | 0.8 | 3.0 | 3.0 | 1.6 |
| $V_R^{(S)}$ | 0.0 | 0.0 | 0 | 0 | 0.0 | 0.0 | − 86.0 |

**Table 3** Parameters for the synaptic currents $I_R^{(T,S)}(t)$ into the MCs (mossy cells) and the HIPP (hilar perforant path-associated) cells. The MCs receive the excitatory inputs from the GCs (granule cells; both mGCs and imGCs) and the inhibitory inputs from the BCs (basket cells) and the HIPP (hilar perforant-associated) cells. The HIPP cells receive the excitatory inputs from the GCs (both mGCs and imGCs) and the MCs

| Target cells ($T$) | MC | | | | HIPP cell | | | |
|---|---|---|---|---|---|---|---|---|
| Source cells ($S$) | GC | | BC | HIPP cell | GC | | MC | |
| Receptor ($R$) | AMPA | NMDA | GABA | GABA | AMPA | NMDA | AMPA | NMDA |
| $K_R^{(T,S)}$ | 9.58 | 1.71 | 3.08 | 2.05 | 0.08 | 0.004 | 4.09 | 0.25 |
| $\tau_{R,r}^{(T,S)}$ | 0.5 | 4.0 | 0.3 | 0.5 | 0.3 | 1.2 | 0.9 | 3.6 |
| $\tau_{R,d}^{(T,S)}$ | 6.2 | 100.0 | 3.3 | 6.0 | 0.6 | 22.2 | 3.6 | 133.7 |
| $\tau_{R,l}^{(T,S)}$ | 1.5 | 1.5 | 1.5 | 1.0 | 1.5 | 1.5 | 3.0 | 3.0 |
| $V_R^{(S)}$ | 0.0 | 0.0 | − 86.0 | − 86.0 | 0.0 | 0.0 | 0.0 | 0.0 |

of individual spiking neurons is done by employing the 2nd-order Runge–Kutta method with the time step 0.1 ms.

## Effect of immature granule cells born via adult neurogenesis on pattern separation

In this section, we study the effect of young adult-born imGCs on pattern separation of the mGCs in our spiking neural network, developed in Sect. 2. Due to high excitability, the imGCs become very active, while because of low excitatory innervation, their activation degree is decreased. We investigate the effects of the two competing properties of the imGCs on the pattern separation efficacy of the mGCs.

### Characterization of pattern separation in the presence of only the mGCs without the imGCs

In this subsection, we first consider the case of presence of only the mGCs (without the imGCs) to present the methods characterizing the pattern separation. As explained in the Sect 2.1, the EC provides external excitatory inputs to the mGCs via PPs [see Fig. 1a] (Myers and Scharfman 2009, 2011; Myers et al. 2013; Scharfman and Myers 2016; Chavlis et al. 2017; Kim and Lim 2022a, 2022b). We characterize pattern separation between the input patterns of the EC cells and the output patterns of the mGCs via integration of the governing equations (1). In each realization, we have a break stage ($0 - 300$ ms) (for which the network reaches a stable state), and then a stimulus stage ($300 - 1,300$ ms) follows; the stimulus period $T_s$ (for which network analysis is done) is 1,000 ms. During the stimulus stage, we get the output firings of the mGCs. For characterization of pattern separation between the input and the output patterns, 30 realizations are made.

The input patterns of the 400 EC cells and the output patterns of the 2,000 mGCs are given in terms of binary representations (Myers and Scharfman 2009; Chavlis et al. 2017); active and silent cells are denoted by 1 and 0, respectively. Here, active cells exhibit at least one spike during the stimulus stage. In each realization, we first make a random choice of an input pattern $A^{(in)}$ for the EC cells, and then construct another input patterns $B_i^{(in)}$ $(i = 1, \ldots, 9)$ from the base input pattern $A^{(in)}$ with the overlap percentage $P_{OL} = 90\ \%, \ldots,$ and 10 %, respectively, as follows (Myers and Scharfman 2009; Chavlis et al. 2017). Among the active EC cells in the pattern $A^{(in)}$, we randomly choose active cells for the pattern $B^{(in)}$ with the probability $P_{OL}$ % (e.g., in the case of $P_{OL} = 60$ %, we randomly choose 24 active EC cells among the 40 active EC cells in the base pattern $A^{(in)}$). The remaining active EC cells in the pattern $B^{(in)}$ are randomly chosen in the subgroup of silent EC cells in the pattern $A^{(in)}$.

We characterize pattern separation between the input and the output patterns by changing the overlap percentage $P_{OL}$. For a pair of input $(l = in)$ or output $(l = out)$ patterns, $A^{(l)}$ and $B^{(l)}$, their pattern distance $D_p^{(l)}$ is given by Chavlis et al. (2017); Kim and Lim (2022c):

$$D_p^{(l)} = \frac{O^{(l)}}{D_a^{(l)}}. \tag{12}$$

Here, $D_a^{(l)}$ is the average activation degree of the two patterns $A^{(l)}$ and $B^{(l)}$:

$$D_a^{(l)} = \frac{(D_a^{(A^{(l)})} + D_a^{(B^{(l)})})}{2}. \tag{13}$$

The average activation degree $D_a^{(l)}$ is just the average one of the activation degrees of the two patterns $A^{(l)}$ and $B^{(l)}$, $D_a^{(A^{(l)})}$ and $D_a^{(B^{(l)})}$. For each pattern, its activation degree is given by the percentage of active cells (represented by "1" in its binary representation). $O^{(l)}$ in Eq. (12) is the orthogonalization degree between $A^{(l)}$ and $B^{(l)}$, denoting their "dissimilarity" degree. Then, as the average activation degree is lower and the orthogonalization degree is higher, the pattern distance between the two patterns $A^{(l)}$ and $B^{(l)}$ increases.

Let $\{a_i^{(l)}\}$ and $\{b_i^{(l)}\}$ $(i = 1, \ldots, N_l)$ be the binary representations [1 (0) for the active (silent) cell] of the two patterns $A^{(l)}$ and $B^{(l)}$ $(l = in$ or $out)$, respectively; $N_{in} = N_{\mathrm{EC}} = 400$ and $N_{out} = N_{\mathrm{GC}} = 2,000$. Then, the Pearson's correlation coefficient $\rho^{(l)}$ between the two patterns $A^{(l)}$ and $B^{(l)}$ is given by

$$\rho^{(l)} = \frac{\sum_{i=1}^{N_l} \Delta a_i^{(l)} \cdot \Delta b_i^{(l)}}{\sqrt{\sum_{i=1}^{N_l} \Delta a_i^{(l)^2}} \sqrt{\sum_{i=1}^{N_l} \Delta b_i^{(l)^2}}}. \tag{14}$$

Here, $\Delta a_i^{(l)} = a_i^{(l)} - \langle a_i^{(l)} \rangle$, $\Delta b_i^{(l)} = b_i^{(l)} - \langle b_i^{(l)} \rangle$, and $\langle \cdots \rangle$ represents population average over all cells; the range of $\rho^{(l)}$ is [-1, 1]. Then, the pattern correlation degree $C^{(l)}$, representing the "similarity" degree between the two patterns, is given just by their Pearson's correlation coefficient $\rho^{(l)}$:

$$C^{(l)} = \rho^{(l)}. \tag{15}$$

Then, the orthogonalization degree $O^{(l)}$, denoting the dissimilarity degree between the two patterns, is given by Kim and Lim (2022c):

$$O^{(l)} = \frac{(1 - \rho^{(l)})}{2}, \tag{16}$$

where the range of $O^{(l)}$ is [0, 1].

With $D_a^{(l)}$ and $O^{(l)}$, we can obtain the pattern distances of Eq. (12), $D_p^{(in)}$ and $D_p^{(out)}$, for the input and the output pattern pairs, respectively. Then, the pattern separation degree $\mathcal{S}_d$, representing the pattern separation efficacy, is given by the ratio of $D_p^{(out)}$ to $D_p^{(in)}$:

$$\mathcal{S}_d = \frac{D_p^{(out)}}{D_p^{(in)}}. \tag{17}$$

If $\mathcal{S}_d > 1$, the output pattern pair of the mGCs is more dissimilar than the input pattern pair of the EC cells, which results in occurrence of pattern separation. Otherwise (i.e., $\mathcal{S}_d < 1$), no pattern separation occurs; instead, pattern "convergence" (i.e., $D_p^{(out)} < D_p^{(in)}$) takes place.

As a sample example, we consider the case of $P_{OL} = 60$ %. Figure 3a1 shows the raster plots of spikes of 400 EC cells (i.e. a collection of spike trains of individual EC cells) for the input patterns $A^{(in)}$ and $B^{(in)}$ for $P_{OL} = 60$ %. In this case, the activation degree $D_a^{(in)}$ is chosen as 10 %, independently of the input patterns. Figure 3a2 shows the raster plots of spikes of 2,000 mGCs for the output patterns $A^{(out)}$ and $B^{(out)}$. As shown well in the raster plots of spikes, the mGCs show sparser firings than the EC cells. In this case, the average activation degree of Eq. (13), $D_a^{(out)}$, is 6 % (which is obtained via 30 realizations). Figure 3b shows the plot of the average activation degree $D_a^{(l)}$ versus the overlap percentage $P_{OL}$; red circles represent the case of input patterns $(l = in)$ and blue crosses denote the case of output patterns $(l = out)$. We note that $D_a^{(out)} = 0.06$ (i.e., 6 %), independently of $P_{OL}$. Then, the sparsity ratio, $\mathcal{R}_s$ $(= D_a^{(in)}/D_a^{(out)})$, becomes

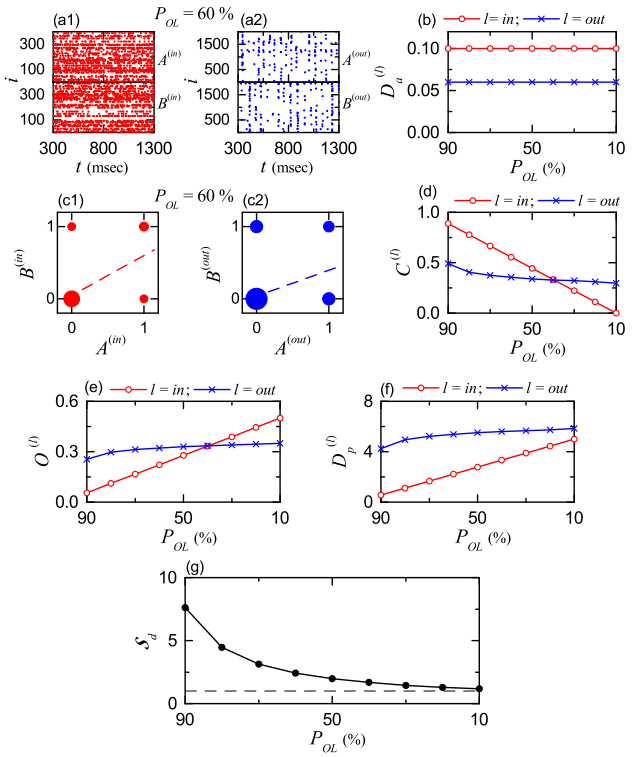


**Fig. 3** Characterization of pattern separation between the input and the output patterns in the presence of only the mGCs without imGCs; $l = in$ (red) and $l = out$ (blue). (**a1**) Raster plots of spikes of ECs for the input patterns $A^{(in)}$ and $B^{(in)}$ in the case of overlap percentage $P_{OL} = 60\%$. (**a2**) Raster plots of spikes of GCs for the output patterns $A^{(out)}$ and $B^{(out)}$. (**b**) Plots of average activation degree $D_a^{(l)}$ versus $P_{OL}$ for the input ($l = in$; red circle) and the output ($l = out$, blue cross) patterns. Plots of the diagonal elements (0, 0) and (1, 1) and the anti-diagonal elements (1, 0) and (0, 1) for the spiking activity (1: active; 0: silent) in the pair of (**c1**) input ($l = in$) and (**c2**) output ($l = out$) patterns $A^{(l)}$ and $B^{(l)}$ for $P_{OL} = 60\%$; sizes of solid circles, located at (0,0), (1,1), (1,0), and (0,1), are given by the integer obtained by rounding off the number of 5 $\log_{10}(n_p)$ ($n_p$: number of data at each location), and a dashed linear least-squares fitted line is also given. Plots of (**d**) average pattern correlation degree $C^{(l)}$, (**e**) average orthogonalization degree $O^{(l)}$, and (**f**) pattern distance $D_p^{(l)}$ versus $P_{OL}$ in the case of the input ($l = in$; red circle) and the output ($l = out$, blue cross) patterns. (**g**) Plot of pattern separation degree $\mathcal{S}_d$ versus $P_{OL}$. (Color figure online)

1.667; the firing activity in the output patterns are 1.667 times as sparse as that in the the input patterns.

Figure 3c1, c2 show plots of the diagonal elements (0, 0) and (1, 1) and the anti-diagonal elements (1, 0) and (0, 1) for the spiking activity (1: active; 0: silent) in the pair of input ($l = in$) and output ($l = out$) patterns $A^{(l)}$ and $B^{(l)}$ for $P_{OL} = 60\%$, respectively. In each plot, the sizes of solid circles, located at (0,0), (1,1), (1,0), and (0,1), are given by the integer obtained by rounding off the number of 5 $\log_{10}(n_p)$ ($n_p$: number of data at each location), and a dashed fitted line is also given. In this case, the Pearson's correlation coefficients of Eq. (14) (obtained via 30 realizations) for the pairs of the input and the output patterns are $\rho^{(in)} = 0.5556$ and $\rho^{(out)} = 0.3550$, which correspond to the slopes of the dashed fitted lines. Then, from Eqs. (15) and (16), we obtain the average pattern correlation degree $C^{(l)}$ and the average orthogonalization degrees $O^{(l)}$ for the pairs of the input and the output patterns; $C^{(in)} = 0.5556$, $C^{(out)} = 0.3550$, $O^{(in)} = 0.2222$ and $O^{(out)} = 0.3225$.

Figures 3d, e show plots of the average pattern correlation degree $C^{(l)}$ and the average orthogonalization degree $O^{(l)}$ versus $P_{OL}$ in the case of the input (red circle) and the output (blue cross) patterns, respectively. Obviously, $C^{(l)}$ and $O^{(l)}$ show oppositely-changing tendencies. Hence, it is enough to discuss only the change in $O^{(l)}$. In the case of the pairs of the input patterns, with decreasing $P_{OL}$ from 90 to 10 % , $O^{(in)}$ increases linearly from 0.0556 to 0.5. On the other hand, in the case of the pairs of the output patterns, $O^{(out)}$ begins from a much larger value (0.2543), but slowly increases to 0.3507 for $P_{OL} = 10$ % (which is lower than $O^{(in)}$). Thus, the two lines of $O^{(in)}$ and $O^{(out)}$ cross for $P_{OL} \simeq 40$ %. Hence, for $P_{OL} > 40$ %, $O^{(out)}$ is larger than $O^{(in)}$ (i.e., the pair of output patterns is more dissimilar than the pair of input patterns). In contrast, for $P_{OL} < 40$ %, $O^{(out)}$ is less than $O^{(in)}$ (i.e., the pair of output patterns becomes less dissimilar than the pair of input patterns).

With the average activation degrees $D_a^{(l)}$ and the average orthogonalization degrees $O^{(l)}$, we can obtain the pattern distances $D_p^{(l)}$ of Eq. (12) for the pairs of input and output patterns. Figure 3f shows plots of the pattern distance $D_p^{(l)}$ versus $P_{OL}$ in the case of the input (red circle) and the output (blue cross) patterns. We note that, for all values of $P_{OL}$, $D_p^{(out)} > D_p^{(in)}$ (i.e., the pattern distance for the pair of output patterns is larger than that for the pair of input patterns). However, with decreasing the overlap percentage $P_{OL}$, the difference between $D_p^{(out)}$ and $D_p^{(in)}$ is found to decrease.

Finally, we obtain the pattern separation degree $\mathcal{S}_d$ of Eq. (17) via the ratio of $D_p^{(out)}$ to $D_p^{(in)}$. Figure 3g shows plots of the pattern separation degree $\mathcal{S}_d$ (representing the pattern separation efficacy) versus $P_{OL}$. As $P_{OL}$ is decreased from 90 % to 10 %, $\mathcal{S}_d$ is found to decrease from 7.6273 to 1.1691. Hence, for all values of $P_{OL}$, pattern separation occurs because $\mathcal{S}_d > 1$. However, the smaller $P_{OL}$ is, the lower $\mathcal{S}_d$ becomes. That is, pattern separation efficacy becomes better for similar input patterns, while for dissimilar input patterns, their pattern separation efficacy becomes worse.

## Effect of the adult-born imGCs on pattern separation

In this subsection, we consider a population, composed of imGCs and mGCs; the fraction of the imGCs in the whole population is 10 %. As shown in Fig. 2, as a result of increased leakage reversal potential $V_L$, the imGC has lower firing threshold than the mGC (i.e., high excitability), which results in high activation of the imGCs (Sahay et al. 2011a, b; Aimone et al. 2011, 2009, 2010; Dieni et al. 2016; Finnegan and Becker 2015). We also note that, the imGC has low excitatory innervation, counteracting the high excitability (Dieni et al. 2016; Finnegan and Becker 2015). In the case of the mGCs, the connection probability $p_c$ from the EC cells and the MCs to the mGCs is 20 %, while in the case of the imGCs, $p_c$ is decreased to 20 $x$ % [$x$ (synaptic connectivity fraction); $0 \le x \le 1$]. Due to low excitatory drive from the EC cells and the MCs, the activation degree of the imGCs becomes reduced. With decreasing $x$ from 1 to 0, we investigate the effect of high excitability and low excitatory innervation of the imGCs on the pattern separation efficacy of the mGCs.

For a given $x$, we consider 9 pairs of input patterns $(A^{(in)}, B_i^{(in)})$ $(i = 1, \ldots, 9)$ with the overlap percentage $P_{OL} = 90$ %, …, and 10 %, respectively. All quantities for the input patterns are independent of $x$. The activation degree $D_a^{(in)}$ is 0.1 (10 %), independently of the pairs. Next, we get the average Pearson's correlation coefficient $\rho^{(in)}$ between the two input patterns in the following way. We first obtain the realization-averaged Pearson's correlation coefficients $\{\langle \rho^{(in)}(i) \rangle_r\}$ ($i = 1, \ldots, 9$ corresponds to $P_{OL} = 90$ %, …, 10 %, respectively) via 30 realizations; $\langle \cdots \rangle_r$ represents the average over 30 realizations. With decreasing $P_{OL}$ from 90 % to 10 %, $\langle \rho^{(in)}(i) \rangle_r$ decreases from 0.8889 to 0.0, respectively. As a representative value, we get the average Pearson's correlation coefficient $\rho^{(in)}$ (= 0.4444), corresponding to the mean of $\{\langle \rho^{(in)}(i) \rangle_r\}$ over all the 9 pairs. Then, from Eqs. (15) and (16), we get the average pattern correlation degree $C^{(in)}$ (= 0.4444) and the average orthogonalization degree $O^{(in)}$ (= 0.2778). In this way, $\rho^{(in)}$, $C^{(in)}$, and $O^{(in)}$ are obtained via double averaging (i.e., averaging over 30 realizations and 9 pairs). Then, the pattern distance $D_p^{(in)}$ of Eq. (12) between the two input patterns (given by the ratio of the average orthogonalization degree to the average activation degree) becomes 2.778.

As in the above case of input patterns, through double averaging over 30 realizations and 9 pairs, we get the average activation degrees $D_a^{(X)}$, the average Pearson's correlation coefficient $\rho^{(X)}$, the average pattern correlation degree $C^{(X)}$, and the average orthogonalization degrees $\mathcal{O}^{(X)}$ in the populations of the imGCs ($X = im$) and the mGCs ($X = m$). Figures 4a, b, c show plots of $D_a^{(X)}$, $C^{(X)}$, and $\mathcal{O}^{(X)}$ versus $x$ [$X = im$ (blue solid circles) and $X = m$ (red open circles)], respectively. Then, we get the pattern distances $D_p^{(X)}$ of Eq. (12) (given by the ratio of $\mathcal{O}^{(X)}$ to $D_a^{(X)}$), which is shown in Fig. 4d. Finally, we obtain the pattern separation degree $\mathcal{S}_d^{(X)}$ of Eq. (17) via the ratio of $D_p^{(out)}$ to $D_p^{(in)}$. Figure 4e shows plots of $\mathcal{S}_d^{(X)}$ versus $x$. As reference lines, horizontal dashed lines, representing $D_a^{(out)}$ (= 6 %), $C^{(out)}$ (= 0.3582), $O^{(out)}$ (= 0.3209), $D_p^{(out)}$ (= 5.3483), and $S_d^*$ (=1.9252) in the presence of only the mGC (without the imGCs) are given in Fig. 4a, b, c, d, e,

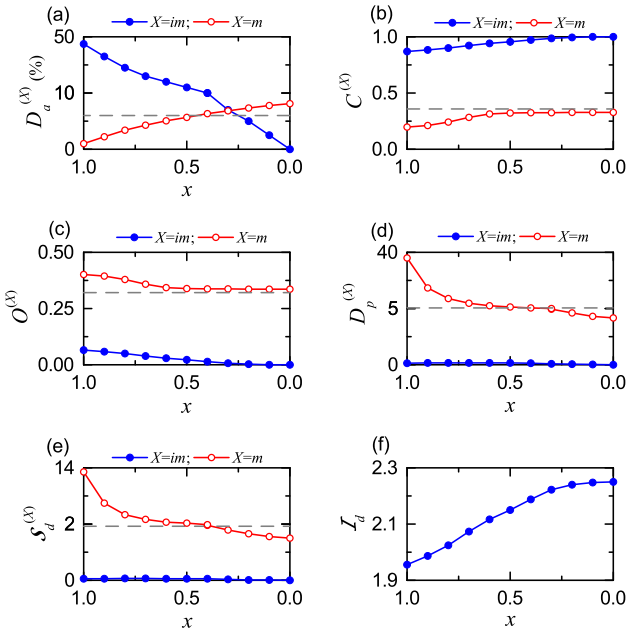


**Fig. 4** Effect of adult-born immature GCs (imGCs) on the pattern separation. (**a**) Plots of the average activation degree $D_a^{(X)}$ versus $x$ (synaptic connectivity fraction). For clear presentation, we choose two different scales for the vertical axis around $D_a^{(X)} = 10$. (**b**) Plots of the average pattern correlation degree $C^{(X)}$ versus $x$. (**c**) Plots of the average orthogonalization degree $O^{(X)}$ versus $x$. (**d**) Plots of the pattern distance $D_p^{(X)}$ versus $x$. For clear presentation, we choose two different scales for the vertical axis around $D_p^{(X)} = 5$. (**e**) Plots of the pattern separation degree $\mathcal{S}_d^{(X)}$ versus $x$. For clear presentation, we choose two different scales for the vertical axis around $\mathcal{S}_d^{(X)} = 2$. In (**a**)–(**e**), imGCs ($X = im$), mGCs ($X = m$), and whole GCs ($X = w$) are denoted by blue solid circles, red open circles, and green crosses, respectively. Horizontal dashed lines in (**a**)–(**e**) represent $D_a^{(out)}$ (= 6 %), $C^{(out)}$ (= 0.3582), $O^{(out)}$ (= 0.3209), $D_p^{(out)}$ (= 5.3483), and $S_d^*$ (=1.9252) in the presence of only mGCs (without imGCs), respectively. (**f**) Plots of the pattern integration degree $\mathcal{I}_d$ of the imGCs versus $x$. (Color figure online)

respectively; these values are obtained via averaging over 9 pairs in Fig. 3.

We first consider the case of $x = 1$ (where the connection probability $p_c$ from the EC cells and the MCs to the imGCs and the mGCs are the same, 20 %), and discuss the effect of the young adult-born imGCs with high excitability on the pattern separation of the mGCs (Aimone et al. 2009, 2010, 2011; Sahay et al. 2011a, b; Finnegan and Becker 2015; Dieni et al. 2016). The imGCs exhibit high activation due to lower firing threshold [i.e., their average activation degree $D_a^{(im)}$ (= 45 %) becomes very high]. As a result, in the population of the imGCs, output patterns become highly overlapped (i.e, their average Pearson's correlation coefficient is very high), which leads to very high average pattern correlation degree $C^{(im)}$ (= 0.8692) and very low average orthogonalization degree $\mathcal{O}^{(im)}$ (= 0.0654). Then, their pattern distance $D_p^{(im)}$ (= 0.145), given by the ratio of $\mathcal{O}^{(im)}$ to $D_a^{(im)}$, also becomes very low. Consequently, the pattern separation degree $\mathcal{S}_d^{(im)}$, given by the ratio of $D_p^{(im)}$ to $D_p^{(in)}$, is 0.052. Since $\mathcal{S}_d^{(im)} < 1$, no pattern separation occurs, due to their high excitability. On the other hand, the efficacy of pattern integration (i.e., making association between patterns) is very high due to high pattern correlation degree $C^{(im)}$. We introduce the pattern integration degree $\mathcal{I}_d$ of the imGCs, given by the ratio of the average pattern correlation degree $C^{(im)}$ to the average pattern correlation degree $C^{(in)}$ for the input patterns:

$$\mathcal{I}_d = \frac{C^{(im)}}{C^{(in)}}, \tag{18}$$

which is in contrast to the pattern separation degree $\mathcal{S}_d$ of Eq. (17). For $x = 1$ the pattern integration degree of the imGCs is high (i.e., $\mathcal{I}_d = 1.9559$). Figure 4f shows plots of $\mathcal{I}_d$ versus $x$ for the imGCs. With decreasing $x$ from 1 to 0, $\mathcal{I}_d$ is increased from 1.9559 to 2.2502, because $C^{(im)}$ increases from 0.8692 to 1. In the whole range of $0 \le x \le 1$, the imGCs are good pattern integrators with $\mathcal{I}_d > 1$.

In contrast, for $x = 1$ the mGCs exhibit very sparse firing activity [i.e., their average activation degree $D_a^{(m)}$ (= 1.1 %) of the mGCs becomes very low] due to strong feedback inhibition from the BCs and the HIPP cells (caused by the high activation of the imGCs); imGC → BC/HIPP → mGC. In this case, the average Pearson's correlation coefficient between the output-pattern pair becomes very low, which leads to high average orthogonalization degree $\mathcal{O}^{(m)}$ (= 0.4016). Then, their pattern distance $P_d^{(m)}$ (= 36.509) becomes very high. Accordingly, the pattern separation degree $\mathcal{S}_d^{(m)}$ is 13.142. Thus, the pattern separation efficacy of the mGCs becomes very high (i.e., the mGCs become good pattern separators), due to high sparsity arising from high excitability of the imGCs.

Next, with decreasing $x$ from 1, we consider the effect of low excitatory innervation for the imGCs, counteracting the effect of high excitability (Dieni et al. 2016; Finnegan and Becker 2015). In the case of mGCs, they receive excitatory inputs from the EC cells and the hilar MCs with the connection probability $p_c$ (= 20 %). On the other hand, the imGCs receive low excitatory drive from the EC cells and the MCs with lower connection probability $p_c$ (= 20 $x$ %) ($x$ : synaptic connectivity fraction; $0 \le x \le 1$). As $x$ is decreased from 1, $D_a^{(im)}$ of the imGCs decreases so rapidly, and their effect becomes weaker. Then, the feedback inhibition to the mGCs is also decreased, and hence $D_a^{(m)}$ of the mGCs becomes increased. In the whole range of $0 \le x \le 1$, the average pattern correlation degree $C^{(im)}$ of the imGCs are very high, and hence they become good pattern integrators with the pattern integration degree $\mathcal{I}_d > 1$ [see Fig. 4f]. On the other hand, due to increase in $D_a^{(m)}$ with decreasing $x$ from 1, the pattern separation efficacy of the mGCs decreases from the high value ($\mathcal{S}_d^{(m)} = 13.142$) for $x = 1$ to a limit value ($\mathcal{S}_d^{(m)} = 1.495$) for $x = 0$.

In the above way, pattern separation efficacy of the mGCs varies through competition between high excitability and low excitatory innervation of the imGCs. In the case that the effect of high excitability is larger than that of low excitatory effect for $1 \ge x > x^*$ ($\simeq 0.4$), the pattern separation of the mGCs becomes enhanced because their pattern separation degree $\mathcal{S}_d^{(m)}$ is larger than $\mathcal{S}_d^*$ (= 1.9253) [i.e., pattern separation degree in the presence of only the mGCs without imGCs, represented by the horizontal dashed line in Fig. 4e]. On the other hand, for $x^* > x \ge 0$, the effect of low excitatory innervation becomes larger than that of high excitability, and hence the pattern separation efficacy of the mGCs becomes worsened because $\mathcal{S}_d^{(m)} < \mathcal{S}_d^*$.

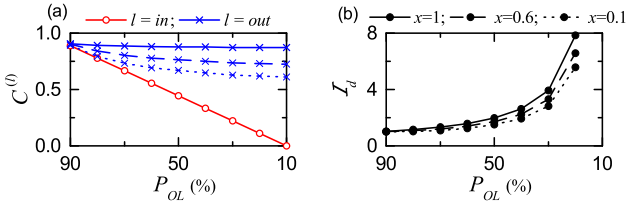


**Fig. 5** Pattern integration in the presence of only imGCs. (**a**) Plots of pattern correlation degrees $C^{(l)}$ versus $P_{OL}$; $l = in$ (red) and $l = out$ (blue). (**b**) Plots of integration degree $\mathcal{I}_d$ versus $P_{OL}$; for $P_{OL} = 10$ % $\mathcal{I}_d$ becomes infinity (not shown) because $C^{(in)} = 0$. In (**a**) and (**b**), the solid, dashed, and dotted lines correspond to the cases of $x = 1$, 0.6, and 0.1, respectively. (Color figure online)

Finally, to more clearly understand the role of the imGCs, we consider a homogeneous population of only the imGCs (without the mGCs), which is in contrast to the case of Sect. 3.1 where population of only mGCs without imGCs is considered. Figure 5a shows the plots of the pattern correlation degree $\mathcal{C}^{(l)}$ versus $P_{OL}$ for the pair of input patterns [$l = in$ (red)] and output patterns [$l = out$ (blue)]; in the case of $l = out$, the solid, dashed, and dotted lines correspond to the cases of $x = 1$, 0.6, and 0.1, respectively. Then, the pattern integration degree $\mathcal{I}_d$ is given by the ratio of $\mathcal{C}^{(out)}$ to $\mathcal{C}^{(in)}$. Figure 5b shows $\mathcal{I}_d$ versus $P_{OL}$. [We note that in the case of $P_{OL} = 10$ %, $\mathcal{C}^{(in)} = 0$, and hence $\mathcal{I}_d$ becomes infinity (not shown).] We note that, as $P_{OL}$ is decreased, $\mathcal{I}_d$ becomes increased, in contrast to the case of $\mathcal{S}_d$ in Fig. 3. Thus, the pattern integration efficacy of the imGCs becomes better for dissimilar input patterns, while it becomes worse for similar input patterns. Hence, the case of pattern integration of the imGCs is in contrast to the case of pattern separation of the mGCs where their pattern separation efficacy becomes better for similar input patterns. We also note that, as $x$ is decreased from 1, the effect of imGCs becomes weaker, leading to decrease in $\mathcal{I}_d$.

## Summary and discussion

We developed a spiking neural network of the DG, composed of mGCs (born during development) and imGCs (born via adult neurogenesis), and investigated the effect of the young adult-born imGCs on the pattern separation of the mGCs. In contrast to the mGCs, the imGCs exhibit two competing distinct properties of high excitability (causing high activation) and low excitatory innervation (reducing activation degree). Due to low excitatory innervation, the connection probability $p_c$ from the excitatory source cells (EC cells and MCs) to the target imGCs is given by 20 $x$ %; $0 \le x \le 1$ ($x$ : synaptic connectivity fraction). Here we are considering imGCs with 3–4 weeks of age. The case of $x = 0$ may be thought to correspond to $\sim$21 days of age. Since then (i.e., with increasing $x$). the degree of synaptic maturity begins to increase.

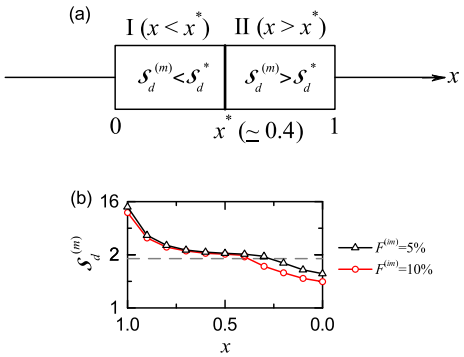


**Fig. 6** (**a**): Diagram for states with lower (I) and higher (II) synaptic maturity. The threshold value, dividing the states I and II, is $x^* \simeq 0.4$. (**b**) Pattern separation degree $\mathcal{S}_d^{(m)}$ of the mGCs for $F^{(im)}$ (fraction of imGCs) = 10 % (red) and 5 % (black). Threshold values $x^* \simeq 0.4$ and 0.27 for $F^{(im)}$ = 10 % and 5 %, respectively. (Color figure online)

The pattern separation degree $\mathcal{S}_d^{(m)}$ of the mGCs was found to vary via competition between high excitability and low excitatory innervation of the imGCs, which is well shown in Fig. 6a. There exist two states I and II, divided at the threshold $x^* (\simeq 0.4)$. The state I corresponds to $0 \le x < x^*$, while the state II corresponds to $x^* < x \le 1$. In the state I with lower synaptic maturity, the effect of low excitatory innervation to the imGCs is larger than the effect of high excitability. Thus, activation degree $D_a^{(im)}$ of the imGCs becomes lower. Then, inhibition to the mGCs (imGC $\rightarrow$ BC/HPP $\rightarrow$ mGC) becomes reduced, leading to increase in the activation degree $D_a^{(m)}$ of the mGCs. Due to such increase in $D_a^{(m)}$, pattern separation degree $S_d^{(m)}$ of the mGCs becomes lower than $\mathcal{S}_d^*$ (=1.9252) in the presence of only mGCs without imGCs. In this way, in the state I (where the effect of low excitatory innervation is dominant), pattern separation of the mGCs becomes worsened. On the other hand, in the state II with higher synaptic maturity, the effect of high excitability becomes larger than the effect of low excitatory innervation. Hence, the activation degree $D_a^{(im)}$ of the imGCs becomes higher, causing strong feedback inhibition to the mGCs. Consequently, the activation degree $D_a^{(m)}$ of the mGCs becomes lower. Due to such sparsity of the mGCs, their pattern separation efficacy becomes enhanced, which seems to be in consistent with experimental results in previous studies (Sahay et al. 2011a, 2011b; Nakashiba et al. 2012).

We also examine the effect of fraction of the imGCs ($F^{(im)}$) on the pattern separation of the mGCs. For comparison, we consider another case of $F^{(im)} = 5$ %. Figure 6b shows plots of the pattern separation degree $\mathcal{S}_d^{(m)}$ versus $x$ (synaptic connectivity fraction) for $F^{(im)} = 10$ % (red) and 5 % (black). We note that these two cases provide similar quantitative results; in the case of 10 % (5 %), the threshold $x^*$ (dividing the two states I and II) is about 0.4 (0.27). Thus, the pattern separation efficacy of the mGCs seems to be insensitive to the fraction of the imGCs ($F^{(im)}$).

In contrast to the mGCs (pattern separators), the young imGCs play the role of good pattern integrators. We also note that the pattern separation efficacy of the mGCs becomes better for similar input patterns, while the pattern integration efficacy of the imGCs becomes better for

dissimilar input patterns. In the homogeneous population of only the mGCs (without the imGCs), memory storage capacity (representing the number of distinct patterns which may be stored and accurately recalled) could be increased with pattern separation efficacy (facilitating the pattern storage and retrieval) (Myers and Scharfman 2009; Chavlis et al. 2017). In contrast, in a heterogeneous population of mGCs (pattern separators) and imGCs (pattern integrators), the memory storage capacity might be optimally maximized via mixed cooperative encoding through pattern separation of the mGCs on similar input patterns and pattern integration of the imGCs on dissimilar input patterns (Aimone et al. 2009, 2010, 2011; Finnegan and Becker 2015; Dieni et al. 2016). Thus, through mixed encoding, memory resolution (corresponding to the extent of information incorporated into memories) could be increased, which would result in reduction in memory interference. This speculation on increase in memory resolution via mixed encoding (through cooperation of pattern separation and pattern integration) must be examined in future works.

Finally, we discuss future works. During pattern separation and pattern integration, sparsely synchronized rhythms appear in the population of the mGCs and the imGCs, respectively. Hence, it would be worthwhile to investigate their population and individual firing behaviors and to discuss their quantitative relationship with the pattern separation and integration efficacy. As in Kim and Lim (2022b, 2022c), population and individual firing behaviors in the sparsely synchronized rhythms in the populations of the mGCs ($X = m$) and the imGCs ($X = im$) may be characterized in terms of the amplitude measure $\mathcal{M}_a^{(X)}$ (representing the population synchronization degree) and the random phase-locking degree $\mathcal{L}_d^{(X)}$ (characterizing the regularity of individual single-cell discharges), respectively. Then, we could investigate the quantitative relationship between $\mathcal{M}_a^{(X)}$ and $\mathcal{L}_d^{(X)}$ of the sparsely synchronized rhythms of the mGCs and the imGCs and the pattern separation degree $\mathcal{S}_d^{(m)}$ of the mGCs and the pattern integration degree $\mathcal{I}_d$ of the imGCs, respectively. Next, we also note that the pyramidal cells in the CA3 provide backprojections to the mGCs via polysynaptic connections (Myers and Scharfman 2011; Myers et al. 2013; Scharfman and Myers 2016). For example, the pyramidal cells send disynaptic inhibition to the mGCs, mediated by the BCs and the HIPP cells in the DG, and they provide trisynaptic inputs to the mGCs, mediated by the MCs (pyramidal cells → MC → BC or HIPP → mGC). These inhibitory backprojections may decrease the activation degree of the mGCs, leading to improvement of pattern separation in the population of the mGCs. Hence, in future work, it would be meaningful to take into consideration the backprojection for the study of pattern separation in the combined DG-CA3 network. Moreover, in the DG-CA3 network, we could examine the memory storage capacity by getting correct response percentage for a partial or noisy version of cue input patterns in the homogeneous population of only the mGCs and in a heterogeneous population of the mGCs and the imGCs (Myers and Scharfman 2011). Then, we could determine which one of the purely sparse encoding (homogeneous case) and the mixed encoding (heterogeneous case) would be superior.

**Acknowledgements** This research was supported by the Basic Science Research Program through the National Research Foundation of Korea (NRF) funded by the Ministry of Education (Grant No. 20162007688).

## References

Aimone JB, Wiles J, Gage FH (2009) Computational influence of adult neurogenesis on memory encoding. Neuron 61:187–202

Aimone JB, Deng W, Gage FH (2010) Adult neurogenesis: integrating theories and separating functions. Trends Cogn Sci 14:325–337

Aimone JB, Deng W, Gage FH (2011) Resolving new memories: a critical look at the dentate gyrus, adult neurogenesis, and pattern separation. Neuron 70:589–596

Almeida LD, Idiart M, Lisman JE (2009) A second function of gamma frequency oscillations: An E%-max winner-take-all mechanism selects which cells fire. J Neurosci 29:7497–7503

Altman J (1962) Are new neurons formed in the brains of adult mammals? Science 135:1127–1128

Altman J (1963) Autoradiographic investigation of cell proliferation in the brains of rats and cats. Anat Rec 145:573–591

Altman J, Das GD (1965) Autoradiographic and histological evidence of postnatal hippocampal neurogenesis in rats. J Comp Neurol 124:319–335

Amaral DG, Witter MP (1989) The three-dimensional organization of the hippocampal formation: a review of anatomical data. Neuroscience 31:571–591

Amaral DG, Ishizuka N, Claiborne B (1990) Neurons, numbers and the hippocampal network. Prog Brain Res 83:1–11

Amaral DG, Scharfman HE, Lavenex P (2007) The dentate gyrus: fundamental neuroanatomical organization (dentate gyrus for dummies). Prog Brain Res 163:3–22

Andersen P, Bliss TVP, Skrede KK (1971) Lamellar organization of hippocampal excitatory pathways. Exp Brain Res 13:222–238

Andersen P, Soleng AF, Raastad M (2000) The hippocampal lamella hypothesis revisited. Brain Res 886:165–171

Bakker A, Kirwan CB, Miller M, Stark CEL (2008) Pattern separation in the human hippocampal CA3 and dentate gyrus. Science 319:1640–1642

Barranca VJ, Huang H, Kawakita G (2019) Network structure and input integration in competing firing rate models for decision-making. J Comput Neurosci 46:145–168

Bartos M, Vida I, Frotscher M, Geiger JR, Jonas P (2001) Rapid signaling at inhibitory synapses in a dentate gyrus interneuron network. J Neurosci 21:2687–2698

Bayer SA (2016) Joseph Altman (1925–2016): a life in neurodevelopment. J Comp Neurol 524:2933–2944

Beck H, Goussakov IV, Lie A, Helmstaedter C, Elger CE (2000) Synaptic plasticity in the human dentate gyrus. J Neurosci 20:7080–7086

Bielczyk NZ, Piskała K, Płomecka M, Radziński P, Todorova L, Foryś U (2019) Time-delay model of perceptual decision making in cortical networks. PLoS One 14:e0211885

Buckmaster PS, Jongen-Rêlo AL (1999) Highly specific neuron loss preserves lateral inhibitory circuits in the dentate gyrus of kainite-induced epileptic rats. J Neurosci 19:9519–9529

Buckmaster PS, Wenzel HJ, Kunkel DD, Schwartzkroin PA (1996) Axon arbors and synaptic connections of hippocampal mossy cells in the rat in vivo. J Comp Neurol 366:271–292

Buckmaster PS, Yamawaki R, Zhang GF (2002) Axon arbors and synaptic connections of a vulnerable population of interneurons in the dentate gyrus in vivo. J Comp Neurol 445:360–373

Cameron HA, Mckay RDG (2001) Adult neurogenesis produces a large pool of new granule cells in the dentate gyrus. J Comp Neurol 435:406–417

Chavlis S, Petrantonakis PC, Poirazi P (2017) Dendrites of dentate gyrus granule cells contribute to pattern separation by controlling sparsity. Hippocampus 27:89–110

Chiang PH, Wu PY, Kuo TW, Liu YC, Chan CF, Chien TC, Cheng JK, Huang YY, Chiu CD, Lien CC (2012) GABA is depolarizing in hippocampal dentate granule cells of the adolescent and adult rats. J Neurosci 32:62–67

Christian KM, Ming GI, Song H (2020) Adult neurogenesis and the dentate gyrus: predicting function from form. Behav Brain Res 379:112346

Coultrip R, Granger R, Lynch G (1992) A cortical model of winner-take-all competition via lateral inhibition. Neural Netw 5:47–54

Dieni CV, Panichi R, Aimone JB, Kuo CT, Wadiche JI, Overstreet-Wadiche L (2016) Low excitatory innervation balances high intrinsic excitability of immature dentate neurons. Nat Commun 7:11313

Dijk van MT, Fenton AA (2018) On how the dentate gyrus contributes to memory discrimination. Neuron 98:832–845

Espinoza C, Guzman SJ, Zhang X, Jonas P (2018) Parvalbumin+ interneurons obey unique connectivity rules and establish a powerful lateral inhibition microcircuit in dentate gyrus. Nat Commun 9:4605

Finnegan R, Becker S (2015) Neurogenesis paradoxically decreases both pattern separation and memory interference. Front Syst Neurosci 9:136

Geiger JRP, Lübke J, Roth A, Frotscher M, Jonas P (1997) Submillisecond AMPA receptor-mediated signaling at a principal neuron-interneuron synapse. Neuron 18:1009–1023

Gerstner W, Kistler W (2002) Spiking neuron models. Cambridge University Press, New York

Gluck MA, Myers CE (2001) Gateway to memory: an introduction to neural network modeling of the hippocampus in learning and memory. MIT Press, Cambridge

Gu Y, Arruda-Carvalho M, Wang J, Janoschka S, Josselyn S, Frankland P, Ge S (2012) Optical controlling reveals time-dependent roles for adult-born dentate granule cells. Nat Neurosci 15:1700–1706

Hafting T, Fyhn M, Molden S, Moser MB, Moser EI (2005) Microstructure of a spatial map in the entorhinal cortex. Nature 436:801–806

Heigele S, Sultan S, Toni N, Bischofberger J (2016) Bidirectional GABAergic control of action potential firing in newborn hippocampal granule cells. Nat Neurosci 19:263–270

Houghton C (2017) Dentate gyrus and hilar region revisited. Behav Brain Sci 39:28–29

Imayoshi I, Sakamoto M, Ohtsuka T, Takao K, Miyakawa T, Yamaguchi M, Mori K, Ikeda T, Itohara S, Kageyama R (2008) Roles of continuous neurogenesis in the structural and functional integrity of the adult forebrain. Nat Neurosci 11:1153–1161

Jahn HM, Bergami M (2018) Critical periods regulating the circuit integration of adult-born hippocampal neurons. Cell Tissue Res 371:23–32

Jahr CE, Stevens CF (1990) Voltage dependence of NMDA-activated macroscopic conductances predicted by single-channel kinetics. J Neurosci 10:3178–3182

Jinde S, Zsiros V, Jiang Z, Nakao K, Pickel J, Kohno K, Belforte JE, Nakazawa K (2012) Hilar mossy cell degeneration causes transient dentate granule cell hyperexcitability and impaired pattern separation. Neuron 76:1189–1200

Jinde S, Zsiros V, Nakazawa K (2013) Hilar mossy cell circuitry controlling dentate granule cell excitability. Front Neural Circ 7:14

Kassab R, Alexandre F (2018) Pattern separation in the hippocampus: distinct circuits under different conditions. Brain Struct Funct 223:2785–2808

Kim SY, Lim W (2022a) Dynamical origin for winner-take-all competition in a biological network of the hippocampal dentate gyrus. Phys Rev E 105:014418

Kim SY, Lim W (2022b) Population and individual firing behaviors in sparsely synchronixed rhythms in the hippocampal dentata gyrus. Cogn Neurodyn 16:643–665

Kim SY, Lim W (2022c) Disynaptic effect of hilar cells on pattern separation in a spiking neural network of hippocampal dentate gyrus. Cogn Neurodyn 16:1427–1447

Kneisler TB, Dingledine R (1995) Spontaneous and synaptic input from granule cells and the perforant path to dentate basket cells in the rat hippocampus. Hippocampus 5:151–164

Knierim JJ, Neunuebel JP (2016) Tracking the flow of hippocampal computation: pattern separation, pattern completion, and attractor dynamics. Neurobiol Learn Mem 129:38–49

Krueppel R, Remy S, Beck H (2011) Dendritic integration in hippocampal dentate granule cells. Neuron 71:512–528

Laplagne DA, Espósito MS, Piatti VC, Morgenstern NA, Zhao C, van Praag H, Gage FH, Schinder AF (2006) Functional convergence of neurons generated in the developing and adult hippocampus. PLOS Biol 4:e409

Laplagne DA, Kamienkowski JE, Esposito MS, Piatti VC, Zhao C, Gage FH, Schinder AF (2007) Similar GABAergic inputs in dentate granule cells born during embryonic and adult neurogenesis. Eur J Neurosci 25:2973–2981

Larimer P, Strowbridge BW (2008) Nonrandom local circuits in the dentate gyrus. J Neurosci 28:12212–12223

Leutgeb JK, Leutgeb S, Moser MB, Moser EI (2007) Pattern separation in the dentate gyrus and CA3 of the hippocampus. Science 315:961–966

Lübke J, Frotscher M, Spruston N (1998) Specialized electrophysiological properties of anatomically identified neurons in the hilar region of the rat fascia dentata. J Neurophysiol 79:1518–1534

Marr D (1971) Simple memory: a theory for archicortex. Phil Trans R Soc Lond B 262:23–81

McNaughton B, Morris R (1987) Hippocampal synaptic enhancement and information storage within a distributed memory system. Trends Neurosci 10:408–415

McNaughton BL, Barnes CA, Mizumori SJY, Green EJ, Sharp PE (1991) Contribution of granule cells to spatial representations in hippocampal circuits: A puzzle. In: Morrell F (ed) Kindling and synaptic plasticity: the legacy of graham goddar. Springer-Verlag, Boston, pp 110–123

Ming GI, Song H (2011) Adult neurogenesis in the mammalian brain: significant answers and significant questions. Neuron 70:687–702

Morgan RJ, Santhakumar V, Soletsz I (2007) Modeling the dentate gyrus. Prog Brain Res 163:639–658

Murray KD, Liu XB, King AN, Luu JD, Cheng HJ (2020) Age-related changes in synaptic plasticity associated with mossy fiber terminal integration during adult neurogenesis. eNeuro 7:1–16

Myers CE, Scharfman HE (2009) A role for hilar cells in pattern separation in the dentate gyrus: a computational approach. Hippocampus 19:321–337

Myers CE, Scharfman HE (2011) Pattern separation in the dentate gyrus: a role for the CA3 backprojection. Hippocampus 21:1190–1215

Myers CE, Bermudez-Hernandez K, Scharfman HE (2013) The influence of ectopic migration of granule cells into the hilus on dentate gyrus-CA3 function. PLoS ONE 8:e68208

Nakashiba T, Cushman JD, Pelkey KA, Renaudineau S, Buhl DL, McHugh TJ, Barrera VR, Chittajallu R, Iwamoto KS, McBain CJ, Fanselow MS, Tonegawa S (2012) Young dentate granule cells mediate pattern separation, whereas old granule cells facilitate pattern completion. Cell 149:188–201

Nitz D, McNaughton B (2004) Differential modulation of CA1 and dentate gyrus interneurons during exploration of novel environments. J Neurophysiol 91:863–872

Nomura T, Fukuda T, Aika Y, Heizmann CW, Emson PC, Kobayashi T, Kosaka T (1997a) Distribution of nonprincipal neurons in the rat hippocampus, with special reference to their dorsoventral difference. Brain Res 751:64–80

Nomura T, Fukuda T, Aika Y, Heizmann CW, Emson PC, Kobayashi T, Kosaka T (1997b) Laminar distribution of non-principal neurons in the rat hippocampus, with special reference to their compositional difference among layers. Brain Res 764:197–204

O'Reilly RC, McClelland JC (1994) Hippocampal conjunctive encoding, storage, and recall: avoiding a tradeoff. Hippocampus 4:661–682

Petrantonakis PC, Poirazi P (2014) A compressed sensing perspective of hippocampal function. Front Syst Neurosci 8:141

Petrantonakis PC, Poirazi P (2015) Dentate gyrus circuitry features improve performance of sparse approximation algorithms. PLoS One 10:e0117023

Ratzliff ADH, Howard AL, Santhakumar V, Osapay I, Soltesz I (2004) Rapid deletion of mossy cells does not result in a hyperexcitable dentate gyrus: implications for epileptogenesis. J Neurosci 24:2259–2269

Rolls ET (1989a) Functions of neuronal networks in the hippocampus and neocortex in memory. In: Byrne JH, Berry WO (eds) Neural models of plasticity: experimental and theoretical approaches. Academic Press, San Diego, pp 240–265

Rolls ET (1989b) The representation and storage of information in neural networks in the primate cerebral cortex and hippocampus. In: Durbin R, Miall C, Mitchison G (eds) The computing neuron. Addition-Wesley, Wokingham, pp 125–159

Rolls ET (1989c) Functions of neuronal networks in the hippocampus and cerebral cortex in memory. In: Cotterill R (ed) Models of brain function. Cambridge University Press, New York, pp 15–33

Rolls ET (2016) Pattern separation, completion, and categorization in the hippocampus and neocortex. Neurobiol Learn Mem 129:4–28

Sahay A, Wilson DA, Hen R (2011a) Pattern separation: a common function for new neurons in hippocampus and olfactory bulb. Neuron 70:582–588

Sahay A, Scobie KN, Hill AS, O'Carroll CM, Kheirbek MA, Burghardt NS, Fenton AA, Dranovsky A, Hen R (2011b) Increasing adult hippocampal neurogenesis is sufficient to improve pattern separation. Nature 472:466–470

Santhakumar V, Aradi I, Soltesz I (2005) Role of mossy fiber sprouting and mossy cell loss in hyperexcitability: a network model of the dentate gyrus incorporating cell types and axonal topography. J Neurophysiol 93:437–453

Santoro A (2013) Reassessing pattern separation in the dentate gyrus. Front Behav Neurosci 7:96

Scharfman HE (2018) Advances in understanding hilar mossy cells of the dentate gyrus. Cell Tissue Res 373:643–652

Scharfman HE, Myers CE (2013) Hilar mossy cells of the dentate gyrus: a historical perspective. Front Neural Circ 6:106

Scharfman HE, Myers CE (2016) Corruption of the dentate gyrus by dominant granule cells: implications for dentate gyrus function in health and disease. Neurobiol Learn Mem 129:69–82

Schmidt B, Marrone DF, Markus EJ (2012) Disambiguating the similar: the dentate gyrus and pattern separation. Behav Brain Res 226:56–65

Schmidt-Hieber C, Bischofberger J (2010) Fast sodium channel gating supports localized and efficient axonal action potential initiation. J Neurosci 30:10233–10242

Schmidt-Hieber C, Jonas P, Bischofberger J (2007) Subthreshold dendritic signal processing and coincidence detection in dentate gyrus granule cells. J Neurosci 27:8430–8441

Sloviter RS, Lømo T (2012) Updating the lamellar hypothesis of hippocampal organization. Front Neural Circ 6:102

Squire L (1987) Memory and brain. Oxford University Press, New York

Su L, Chang CJ, Lynch N (2019) Spike-based winner-take-all computation: fundamental limits and order-optimal circuits. Neural Comput 31:2523–2561

Toni N, Teng EM, Bushong EA, Aimone JB, Zhao C, Consiglio A, van Praag H, Martone ME, Ellisman MH, Gage FH (2007) Synapse formation on neurons born in the adult hippocampus. Nat Neurosci 10:727–734

Toni N, Laplagne DA, Zhao C, Lombardi G, Ribak CE, Gage FH, Schinder AF (2008) Neurons born in the adult dentate gyrus form functional synapses with target cells. Nat Neurosci 11:901–907

Treves A, Rolls ET (1991) What determines the capacity of auto associative memories in the brain? Network 2:371–397

Treves A, Rolls ET (1992) Computational constraints suggest the need for two distinct input systems to the hippocampal CA3 network. Hippocampus 2:189–199

Treves A, Rolls ET (1994) Computational analysis of the role of the hippocampus in memory. Hippocampus 4:374–391

van Praag H, Schinder AF, Christie BR, Toni N, Palmer TD, Gage FH (2002) Functional neurogenesis in the adult hippocampus. Nature 415:1030–1034

Wang Y, Zhang X, Xin Q, Hung W, Florman J, Huo J, Xu T, Xie Y, Alkema MJ, Zhen M, Wen Q (2020) Flexible motor sequence generation during stereotyped escape responses. eLife 9:e56942

West MJ, Slomianka L, Gundersen HJ (1991) Unbiased stereological estimation of the total number of neurons in the subdivisions of the rat hippocampus using the optical fractionator. Anat Rec 231:482–497

Willshaw D, Buckingham J (1990) An assessment of Marr's theory of the hippocampus as a temporary memory store. Phil Trans R Soc Lond B 329:205–215

Yassa MA, Stark CEL (2011) Pattern separation in the hippocampus. Trends Neurosci 34:515–525

Yim MY, Hanuschkin A, Wolfart J (2015) Intrinsic rescaling of granule cells restores pattern separation ability of a dentate gyrus network model during epileptic hyperexcitability. Hippocampus 25:297–308